PREVIEW RIT'S LATEST & GREATEST SOFTWARE VERSION AT THE

ASTRO 2020 VIRTUAL MEETING

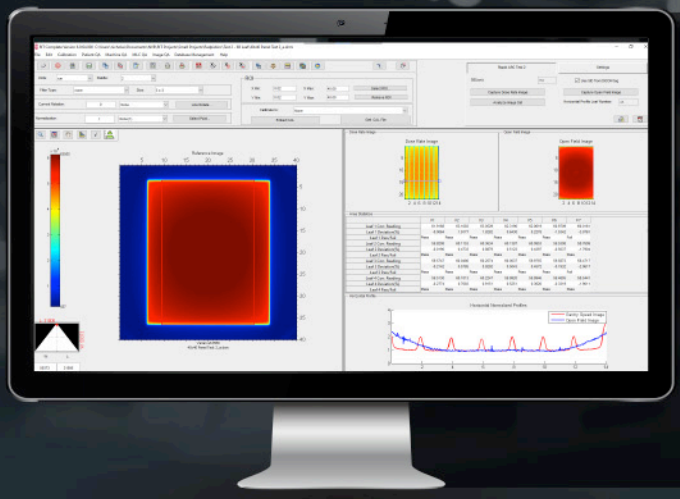

Radiological Imaging Technology, Inc. offers QA software solutions for every medical physicist. Find your perfect software package at our booth in the ASTRO Virtual Meeting exhibit hall from **October 23–29, 2020**. *Request a personalized demonstration to get an exclusive preview of RIT's latest software upgrade,* ***Version 6.9 of the RIT Family of Products****, soon to be released.*

PREVIEW THESE INNOVATIVE FEATURES FROM OUR NEW SOFTWARE UPGRADE

THE RIT FAMILY OF PRODUCTS - VERSION 6.9

- Utilize the 60-Leaf MLC analysis for Varian RapidArc® tests, which allows for expanded support of a wider range of Varian LINACs.
- Perform couch placement analysis for PTW EPID and Primus®-L phantoms, providing an analysis that is closer to realistic patient positioning.
- Perform enhanced TomoTherapy® Registration, now with expanded support for additional Accuray treatment planning systems.
- Enjoy increased flexibility on acceptance criteria (TG-58 or Varian QA guidelines) when analyzing images from the Las Vegas EPID phantom.
- In the CATPHAN® Low Contrast module, select among Contrast-to-Noise analysis options for the phantom.
- Use the new DICOM Anonymizer feature to automatically remove sensitive and confidential medical information from any DICOM file.
- Utilize floating license capability, local to your facility's network with the Local License Server license configuration option.
- Perform diagnostic TOR-18 phantom analysis on images captured with high-resolution fluoroscopy machines.

CLICK TO EXPLORE OUR VIRUAL BOOTH

RIT®

RADIMAGE.COM

+1.719.351.1399 // sales@radimage.com // Connect with RIT on social media @RIT4QA

Technical and dosimetric realization of *in vivo* x-ray microbeam irradiations at the Munich Compact Light Source

Karin Burger and Theresa Urban
Department of Radiation Oncology, School of Medicine & Klinikum rechts der Isar, Technical University of Munich, Munich 81675, Germany
Chair of Biomedical Physics, Department of Physics and Munich School of BioEngineering, Technical University of Munich, Garching 85748, Germany

Annique C. Dombrowsky
Department of Radiation Oncology, School of Medicine & Klinikum rechts der Isar, Technical University of Munich, Munich 81675, Germany
Institute of Radiation Medicine (IRM), Department of Radiation Sciences (DRS), Helmholtz Zentrum München, Neuherberg 85764, Germany

Martin Dierolf and Benedikt Günther
Chair of Biomedical Physics, Department of Physics and Munich School of BioEngineering, Technical University of Munich, Garching 85748, Germany

Stefan Bartzsch
Department of Radiation Oncology, School of Medicine & Klinikum rechts der Isar, Technical University of Munich, Munich 81675, Germany
Institute of Radiation Medicine (IRM), Department of Radiation Sciences (DRS), Helmholtz Zentrum München, Neuherberg 85764, Germany

Klaus Achterhold
Chair of Biomedical Physics, Department of Physics and Munich School of BioEngineering, Technical University of Munich, Garching 85748, Germany

Stephanie E. Combs and Thomas E. Schmid
Department of Radiation Oncology, School of Medicine & Klinikum rechts der Isar, Technical University of Munich, Munich 81675, Germany
Institute of Radiation Medicine (IRM), Department of Radiation Sciences (DRS), Helmholtz Zentrum München, Neuherberg 85764, Germany

Jan J. Wilkens[a)]
Department of Radiation Oncology, School of Medicine & Klinikum rechts der Isar, Technical University of Munich, Munich 81675, Germany
Chair of Biomedical Physics, Department of Physics and Munich School of BioEngineering, Technical University of Munich, Garching 85748, Germany

Franz Pfeiffer
Chair of Biomedical Physics, Department of Physics and Munich School of BioEngineering, Technical University of Munich, Garching 85748, Germany
Department of Diagnostic and Interventional Radiology, School of Medicine & Klinikum rechts der Isar, Technical University of Munich, München 81675, Germany

(Received 11 December 2019; revised 15 April 2020; accepted for publication 20 July 2020; published xx xxxx xxxx)

Purpose: X-ray microbeam radiation therapy is a preclinical concept for tumor treatment promising tissue sparing and enhanced tumor control. With its spatially separated, periodic micrometer-sized pattern, this method requires a high dose rate and a collimated beam typically available at large synchrotron radiation facilities. To treat small animals with microbeams in a laboratory-sized environment, we developed a dedicated irradiation system at the Munich Compact Light Source (MuCLS).
Methods: A specially made beam collimation optic allows to increase x-ray fluence rate at the position of the target. Monte Carlo simulations and measurements were conducted for accurate microbeam dosimetry. The dose during irradiation is determined by a calibrated flux monitoring system. Moreover, a positioning system including mouse monitoring was built.
Results: We successfully commissioned the *in vivo* microbeam irradiation system for an exemplary xenograft tumor model in the mouse ear. By beam collimation, a dose rate of up to 5.3 Gy/min at 25 keV was achieved. Microbeam irradiations using a tungsten collimator with 50 μm slit size and 350 μm center-to-center spacing were performed at a mean dose rate of 0.6 Gy/min showing a high peak-to-valley dose ratio of about 200 in the mouse ear. The maximum circular field size of 3.5 mm in diameter can be enlarged using field patching.

Conclusions: This study shows that we can perform *in vivo* microbeam experiments at the MuCLS with a dedicated dosimetry and positioning system to advance this promising radiation therapy method at commercially available compact microbeam sources. Peak doses of up to 100 Gy per treatment seem feasible considering a recent upgrade for higher photon flux. The system can be adapted for tumor treatment in different animal models, for example, in the hind leg. [https://doi.org/10.1002/mp.14433]

Key words: compact synchrotron source, inverse Compton source, microbeam dosimetry, microbeam radiation therapy, preclinical study, small animal RT

1. INTRODUCTION

In the last three decades, various experimental, preclinical studies on x-ray microbeam radiation therapy (MRT) have shown treatment effects often superior to those achieved by conventional radiation therapy with homogeneous broad beams. In the last two decades, various studies on x-ray microbeam radiation therapy (MRT) have shown its beneficial treatment effect compared to conventional homogeneous radiation therapy.[1–5] To widen the therapeutic window, the x-ray beam is subdivided by an absorbing grid into an array of periodic parallel beams tens of micrometers wide separated by about 200–400 μm. Doses of several hundreds of Gray in the microbeam peaks are well tolerated by the normal tissue in case kiloelectronvolt (keV) x rays are applied and hence the range of scattered secondary electrons is short. Microbeams spare normal tissues, notably normal blood vessels.[3,6] Conversely, it has been shown that the destruction of tumor vascular systems by microbeams is relevant for the therapeutic effect.[7–10] Further research on microbeam radiation effects *in vivo*, particularly on vessels, is required. To avoid motion-induced blurring of the microbeam pattern, a high dose rate of about 100 Gy/s or higher is essential to achieve irradiation times below 1 s.[11–13] Moreover, a well-collimated beam allows to achieve a low valley dose. Due to these strong requirements of x-ray beam properties, MRT has mainly been developed at a few large synchrotron facilities worldwide and access for future patient treatment will be limited. Additionally to the use of conventional x-ray tubes for MRT experiments *in vitro*,[14] different designs for smaller x-ray sources have been tested or proposed,[15–17] which demonstrates the need of such a compact tool. Here, we used the Munich Compact Light Source (MuCLS), a compact synchrotron based on the concept of inverse Compton scattering with relatively low operational costs.[18] In previous work, it was shown that microbeam irradiations of normal tissue cells *in vitro* reduced the number of chromosomal aberrations and increased cell survival compared to homogeneously irradiated cells.[19] Consequently, a dedicated setup for *in vivo* experiments with small animals at a laboratory-sized x-ray source was built for preclinical studies on MRT. It shapes the beam, performs online dosimetry, and accurately positions and controls the animal. We validate the setup by irradiating tumors xenografted in mouse ears. The performance and possible applications of the setup are analyzed and discussed.

In previous work, it was shown that microbeam irradiations *in vitro* lead to a reduced number of chromosomal aberrations and an increased cell survival compared to homogeneously irradiated normal tissue cells. Following these promising results, a dedicated setup for *in vivo* experiments with small animals was built. Such a system allows to perform preclinical studies on MRT at a laboratory-sized x-ray source in order to better understand the radiobiological effects of MRT. In this study, we present a dedicated microbeam irradiation setup installed at the MuCLS to shape the beam, perform online dosimetry, and accurately position and control the animal. We validated the setup using a tumor model in the mouse ear. The performance and possible applications of the setup are analyzed and discussed.

2. MATERIALS AND METHODS

The Compact Light Source (CLS, Lyncean Technologies Inc., USA) is a laboratory-sized synchrotron using the principle of inverse Compton scattering. In our system, the collision of infrared laser pulses with highly energetic electron bunches creates x rays in the range of 15–35 keV; details can be found in Achterhold et al., 2013[20] and Eggl et al., 2016.[18] Up to 3×10^{10} ph/s are emitted with a beam divergence of ± 2 mrad, having an almost monochromatic energy spectrum of about 4% bandwidth. The system has a footprint of $3 \times 5\ m^2$.

Figure 1 depicts a schematic drawing of the microbeam irradiation setup in the experimental hutch of the MuCLS. We focused the photon flux for microbeam irradiations using a dedicated polycapillary optic (Institute for Scientific Instruments GmbH, Germany) placed at 1.8 m to the source.

For online dose monitoring, a scintillation counter was installed to control the flux in front of the sample. An inclined 7-μm thin polyethylene foil scatters a tiny fraction of the photons onto a scintillator-based detector system installed at 90° to the beam path. This relative intensity counter is calibrated with a photon counting detector (Pilatus 200K, Dectris, Switzerland) to collect absolute online information on the x-ray flux. Downstream of the scintillation counter, an aperture shapes the beam. For microbeam irradiations, different gratings can be inserted to create spatially separated beamlets. Here, we show irradiations of tumors grown in the mouse ear. The mouse ear was positioned directly downstream of the aperture. Additionally to the online dose monitoring system, radiochromic films (Gafchromic EBT3,

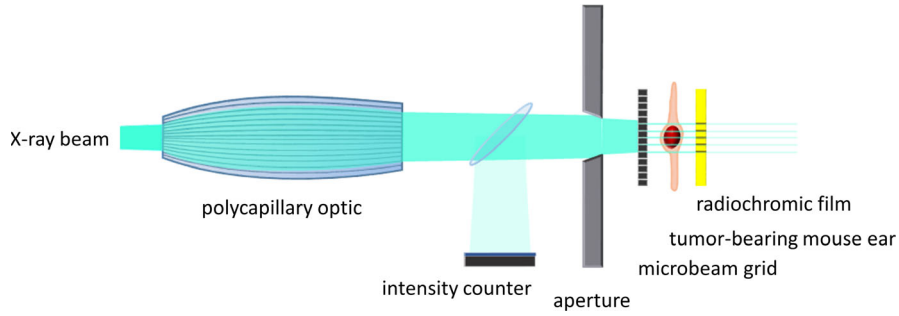

FIG. 1. Schematic drawing of the x-ray beam path for *in vivo* microbeam irradiations at the Munich Compact Light Source (MuCLS).

Ashland, USA) were placed on the back of the mouse ear to verify the given dose.

This *in vivo* study was approved by the ethics committee of the government of Upper Bavaria (reference number 55.2.1.54-2532-62-2016). Xenograft tumors were grown in nude NMRI nu/nu mice from subcutaneously injected FaDu cells (head-and-neck cancer cell line) suspended in Matrigel following the protocol of Oppelt et al.[21] Irradiation is performed when the tumor reaches a minimum diameter of 2 mm in the ear plane (details can be found in[22,23]).

Due to the small tumor size, precise positioning is highly important. Thus, the mouse ear was aligned to the beam using motorized stages with semi-automatic control. The 215–250 μm thin,[23] low-absorbing ear allows to easily control the tumor position by a CCD camera system.

3. RESULTS

Here, we show the characteristics and performance of the main components necessary for microbeam irradiations at the MuCLS: the shaped x-ray beam, the dosimetry system as well as the positioning and treatment of the tumor.

3.A. Collimating polycapillary optic

We maximized the x-ray flux for small animal irradiations with a sample size of a few mm. At the MuCLS, experiments can be performed at a minimum distance of about 4 m downstream of the source, where the field of view extends to a diameter of 16 mm. Thus, a collimation or focusing system is required to efficiently exploit the available photons.

To account for the small energy bandwidth of the CLS spectra of about 4% and to be compatible with the different energies that can be chosen at the CLS, the optic has to provide a reasonably high efficiency over a broad energy range. This means that losses due to its insertion need to be overcompensated by the increase in fluence rate in the desired irradiation area. Additionally, the device must accept the divergence angle of the cone of 4 mrad and offer an entrance diameter of at least 7 mm. For an installation of the optic in the cave, the current setup requires a focus distance of about 2 m and a device length below 20 cm. These requirements can be fulfilled by polycapillary optics consisting of bundles of capillaries through which the x rays travel by external reflection. As the above-mentioned parameters differ from standard x-ray tube setups or synchrotron radiation facilities, a dedicated optic was designed (Institute for Scientific Instruments GmbH, Germany).

The performance of a polycapillary optic about 62 mm long (L), with entrance/exit diameters: $D_{in} = 11.85$ / $D_{out} = 11.95$ mm is presented as an example. The D_{in} of the optic was positioned at $f_{in} = 1.8$ m downstream of the source, equivalent to the input focal distance. A schematic drawing (not to scale) of the x-ray path through the optic is shown in Fig. 2(a). The dose distribution at the entrance of the polycapillary optic was measured with a radiochromic film, see Fig. 2(b). Figure 2(d) shows the central horizontal (blue) and vertical (red) line profile. To align the optic, a raster scan was carried out by linear movement and tilt of the optic in horizontal and vertical direction perpendicular to the beam axis. The focal spot quality in terms of intensity and shape was determined by direct imaging at the output focal distance $f_{out} = 2$ m using an Andor Zyla 5.5 sCMOS camera (Oxford Instruments, United Kingdom) with a fiber-optically coupled scintillator (6.5×6.5 μm^2 pixel size) and by indirect imaging of the focal spot propagated by about 12.5 m using the Pilatus 200K photon-counting detector. To stay below the saturation limit of the sCMOS camera, the x-ray beam flux was reduced by a slight misalignment of electron bunch and laser pulse collision. Figure 2(c) shows the direct image of the focal spot with the corresponding central horizontal (blue) and vertical (red) line profiles in Fig. 2(e). The data were processed with a median filter (kernel size of 15) to reduce noise which had negligible influence on the quantitative analysis. By fitting a Gaussian to the data, the full width at half maximum (FWHM) of the focal spot in both horizontal and vertical direction was determined to 2.5 and 2.7 mm, respectively. Finally, the FWHM values were corrected for the point-spread function of the camera system of about 11.5 μm[24] by applying a Richardson–Lucy deconvolution algorithm.[25] Thus, the actual focal spot reaches 2 mm in horizontal and 2.3 mm in vertical direction. To cover larger field sizes in the range of 3.5 mm in diameter, a second polycapillary optic is available (not shown here).

Furthermore, we determined the efficiency of the polycapillary optic for the 25 keV energy configuration at the MuCLS. The transmission of the optic was measured by

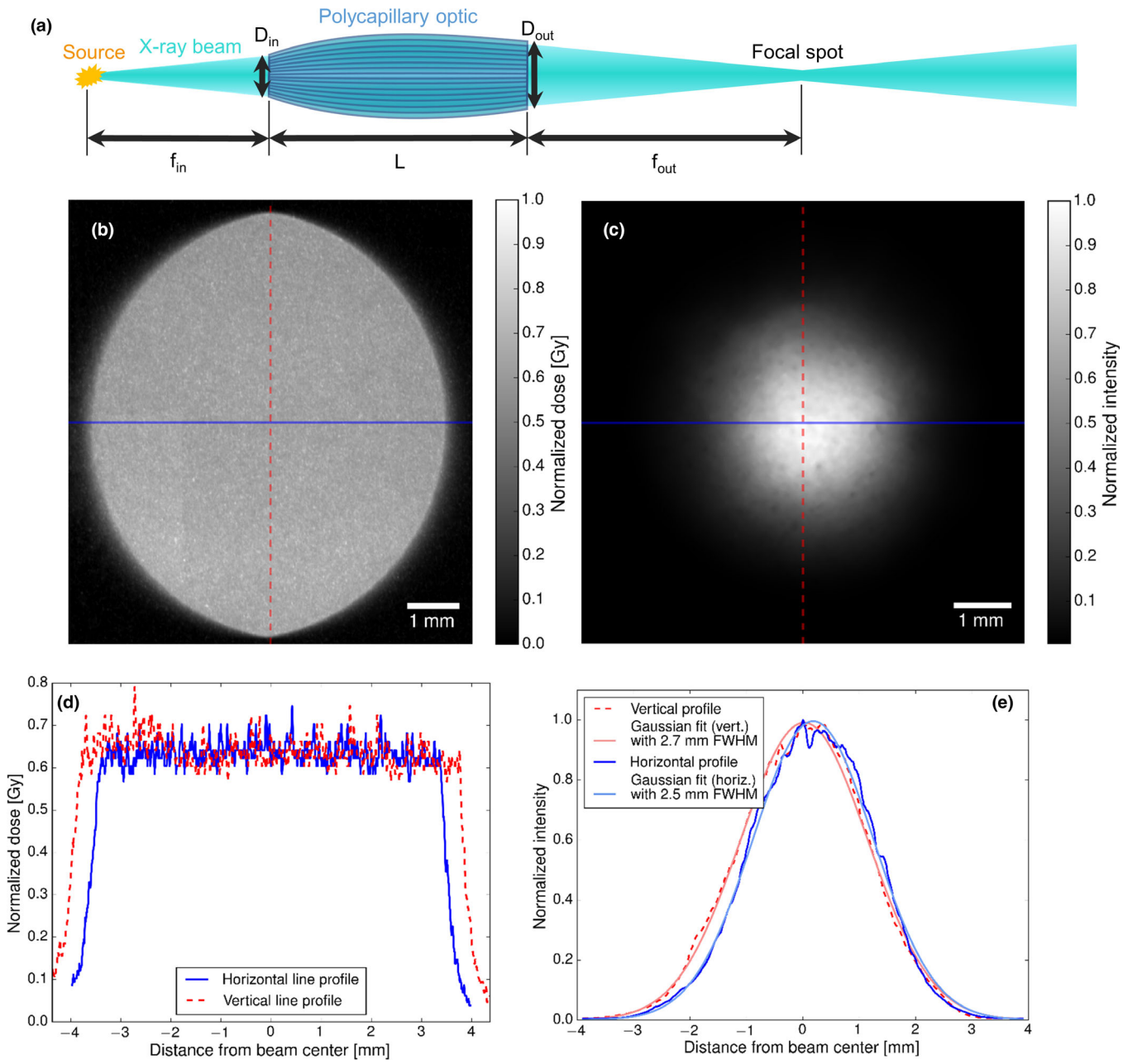

FIG. 2. (a) Schematic drawing of the polycapillary optic for x-ray beam shaping (not to scale). (b) At the entrance position, the x-ray dose was measured with a radiochromic film. (c) At the focal spot, a camera system recorded the intensity distribution. Accordingly, horizontal (blue) and vertical (red) line profiles from the center of both images are shown in (d) and (e).

comparing the total photon flux with and without optic. For this purpose, the calibrated scintillation counter was placed in front of the camera system. Thus, the absolute number of photons per second was monitored allowing to correct for alternating flux during the measurement. We measured the transmission of the described optic to 44% of the incoming x rays. According to the results above, we assumed these photons to be confined within an ellipse of $1 \times 1.15 \times \pi\,\mathrm{mm}^2 (3.6\,\mathrm{mm}^2)$. The untreated beam extends at the focal position to $7 \times 8.25 \times \pi\,\mathrm{mm}^2$ $(181.4\,\mathrm{mm}^2)$. In conclusion, this polycapillary optic permits to enhance the x-ray intensity by a factor of 22.

3.B. Setup for *in vivo* irradiations

We demonstrate the performance of the microbeam irradiation setup for an exemplary treatment of a tumor xenografted to a mouse ear. This tumor model is well-suited to the setup parameters of the CLS. Figure 3 shows photographs of the experimental setup. In the left image, the pink, dotted line represents the x-ray beam path. The beam exits from the cave into the experimental hutch through a beam pipe. For constant flux monitoring, the scintillation counter is installed in front of the sample. Downstream of the counter, the beam aperture made of stainless steel is positioned, which is mounted together with the

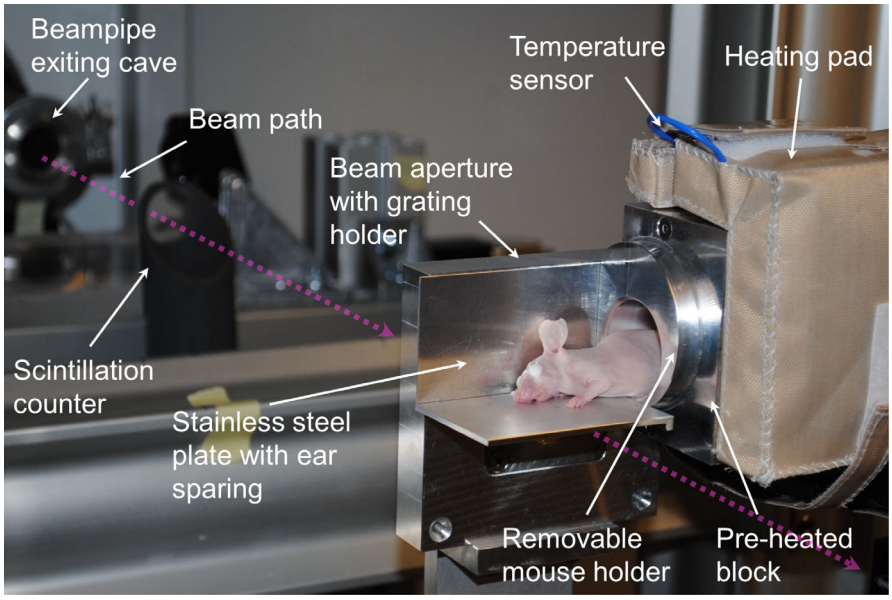

FIG. 3. Photographs of the microbeam irradiation setup for treatment of xenograft tumors in the mouse ear. The left image shows the individual setup components. The x-ray beam path is presented as a pink, dotted line. The upper and lower right images show front and back side of the removable mouse holder. The exposed mouse ear bearing a tumor at the center is visible from the front side (reddish spot on mouse ear). A radiochromic film was placed downstream of the mouse ear, as seen at the back side.

mouse holder (see below) on a rotation axis for alignment perpendicular to the optical axis and on two linear stages to optimize its position with respect to the focal spot given by the polycapillary optic.

With the currently available 3 mm diameter circular and $1.5 \times 1.5\,\text{mm}^2$ quadratic apertures, different irradiation field sizes can be chosen (visible in Fig. 4). The quadratic aperture can be used to irradiate larger tumors by patching several irradiation fields to each other. The fields are irradiated separately and the tumor is repositioned in-between using the motorized stages, causing a time delay <1 min. The positioning is performed such that the neighboring borders of two fields lie within the FWHM of the focal spot to keep the dose as homogeneous as possible throughout the field. Figure 4(e) shows a radiochromic film irradiated with a stitched microbeam field.

For microbeam irradiations, a grating is inserted in an accurately sized carving on the back side of the aperture, which enables repeatable positioning of the absorbing grid in the x-ray beam path. Different $1 \times 1\,\text{cm}^2$ gratings made of 200−μm thick tungsten are available (fabricated by laser

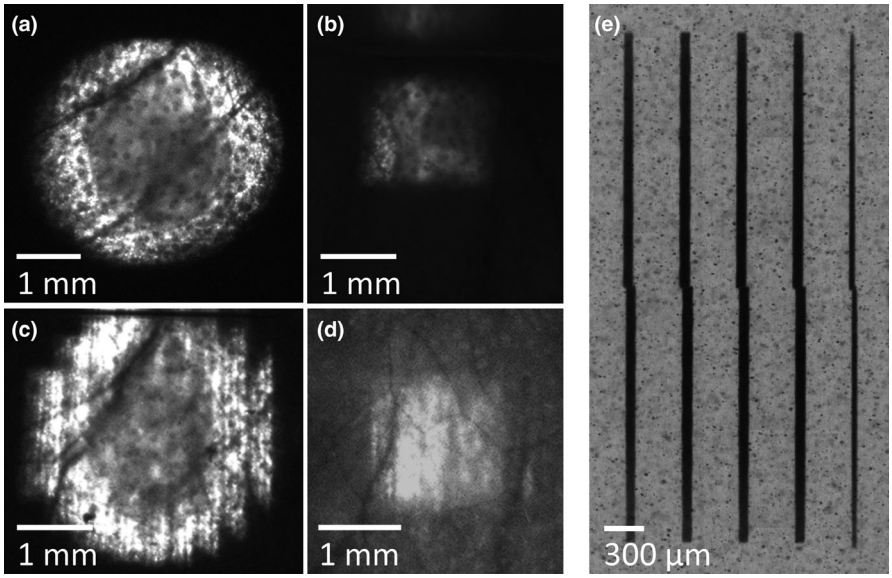

FIG. 4. Tumor positioning for the mouse ear model with a CCD camera. Following the described procedure, tumors in (a)–(d) were centered using (a) an open circular field, (b) an open quadratic field, (c) a circular field with grating and (d) a quadratic field with grating. (e) shows an image of the irradiated radiochromic film with microbeams using field patching.

micro-machining, Laser Micromachining Ltd., UK). So, the microbeam width can be changed on the order of tens of micrometers, while the spacing is variable on the order of hundreds of micrometers. Here, a 50−μm slit size with a center-to-center spacing of 350 or 400 μm is used, yielding a maximum dose rate of 0.6 Gy/min.

To shield the mouse head from scattered x rays, a stainless steel plate with ear sparing was constructed (see Fig. 3). The mouse ear can be fixed with removable tape on the plate to avoid any motion of the tumor. The body of the mouse is placed in a heatable aluminum cylinder. This mouse holder is installed on three additional translational stages to ideally position the tumor-bearing mouse ear in the x-ray beam. In particular, the distance to the grating is minimized to avoid blurring of the microbeam pattern. To maintain the mouse body temperature during anesthesia, a heating pad, covering the mouse holder, is operated at a temperature of about 32°C. A webcam allows to monitor breathing motion during irradiation. Positioning and heating are controlled from outside the experimental hutch. Due to the transparency of the mouse ear, the positioning of the tumor in the field of view is achieved by a transmission image in visible light [Figs. 4(a)–4(d)]. The image is recorded with a macroCCD camera such that the mouse ear can easily be moved to the desired position using the externally controlled motors.

If necessary, a fast shutter and direct control of the CLS allow to stop the irradiation in less than two seconds. Following an interruption, the software evaluates the partial dose given to the tumor and the irradiation can be continued to deliver the remaining requested dose.

3.C. Microbeam characterization

We performed experimental and simulation studies to accurately determine the microbeam dose profile produced by the above-shown setup at the MuCLS. One important characteristic for microbeam dosimetry is the so-called peak-to-valley dose ratio (PVDR) as the peak dose must be high enough to cause vascular damage to the tumor and the valley dose low enough to achieve a sparing effect in the normal tissue.[9] Here, the PVDR is determined by film dosimetry validated by Monte Carlo simulations.

3.C.1. Film dosimetry

The experimental measurement was performed using Gafchromic EBT3 films. Films were calibrated at a conventional irradiation system (Small Animal Radiation Research Platform (SARRP), xstrahl Ltd, UK) with a sufficient field size and dose rate following the recommended protocol.[26] To test film response for its spectral dependence, 30 and 50 kVp x-ray spectra were used for the calibration at the SARRP. The film response differed by less than 1% for the two x-ray peak energies, much less than overall calibration uncertainty of 3.3% given by the ionization chamber (TM23342, PTW, Germany). Therefore, we assumed that the calibration at the SARRP is also valid for the 25-keV MuCLS spectrum.

In MRT, peak and valley doses differ by several orders of magnitude. Since radiochromic films can only cover up to one order of magnitude in dose difference, irradiation of two separate films with adapted exposure times is necessary to determine the peak and valley doses, respectively. Films were taped to 1.6-mm thick PMMA slabs, which allowed to account for x-ray scattering within the irradiation sample, here the mouse ear. For irradiation, the films were positioned 4 mm downstream of the grating. Subsequently, the films were read out with an optical microscope following Bartzsch et al.[27] The resulting dose distributions from both films were rescaled by their relative exposures and merged (cf. Section 3.C.3).

3.C.2. Simulation

The simulation of the dose distribution was carried out with the Geant 4 Monte Carlo simulation toolkit version 10.0 using the Livermore physics libraries.[28] Source shape and size were implemented by sampling the initial photon positions from a Gaussian distribution with 45 μm standard deviation. Initial particle directions were homogeneously distributed with a divergence of ±2 mrad following the beam characteristics of the CLS.[18] For the energy distribution of the x rays, the spectrum at the 25-keV configuration was measured and included in the particle generation. Additionally, the silicon and beryllium exiting windows and the stainless steel beam pipe in the CLS cave were implemented. The focusing optic with a focus size of $3.3 \times 3.7\,\mathrm{mm}^2$ was simulated by manually changing particle directions according to the optics specifications. The polyethylene foil, the aperture, and the grating (see Fig. 1) were also included. A slit width of 50 μm and a center-to-center spacing of 400 μm were chosen. The film was implemented as a 280-μm thick layer of polymer mimicking the film composition, and positioned 4 mm downstream of the grating like in the *in vivo* experiments.

3.C.3. Comparison of simulated and experimental data

The simulated and measured dose distributions are shown in Fig. 5. The central profile of the measured dose distribution is illustrated in Fig. 6.

While the peak doses follow the uncollimated beam shape with a FWHM of 3.3 mm in the direction perpendicular to the microbeams, the valley doses have a broader distribution due to x-ray scattering. This leads to a PVDR highest in the center and decreasing towards outer areas of the beam.

For comparison of simulation and measurement, a zoom into both the dose profiles and the dose histograms is shown in Fig. 7. The width and height of the peaks and valleys in the dose profiles in Fig. 7(a) match very well, and the histograms (Fig. 7(b)) show a clear separation of peak and valley doses.

Since the peak and valley doses vary over the field of view, the overall PVDR was calculated using the cumulative dose histogram [see Fig. 7(c)]. The peak dose was defined as the dose that 60% of the peak area, that is 60%·1/8 = 7.5%

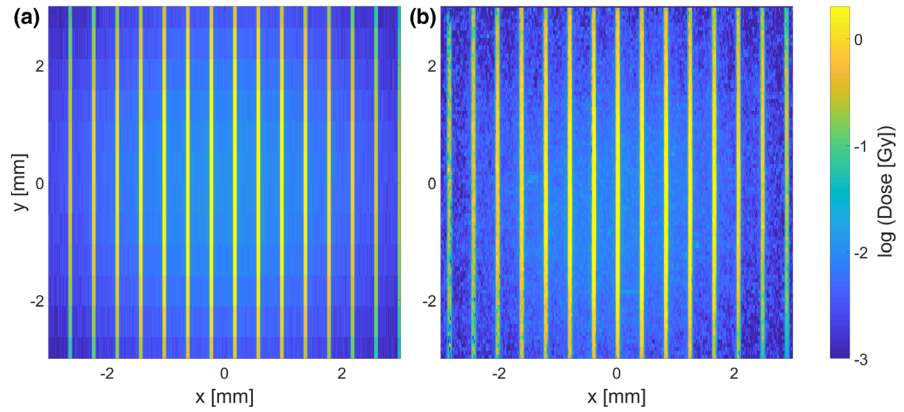

FIG. 5. In (a), the simulated dose distribution is shown. The measured dose distribution in (b) represents a combination of peak and valley film.

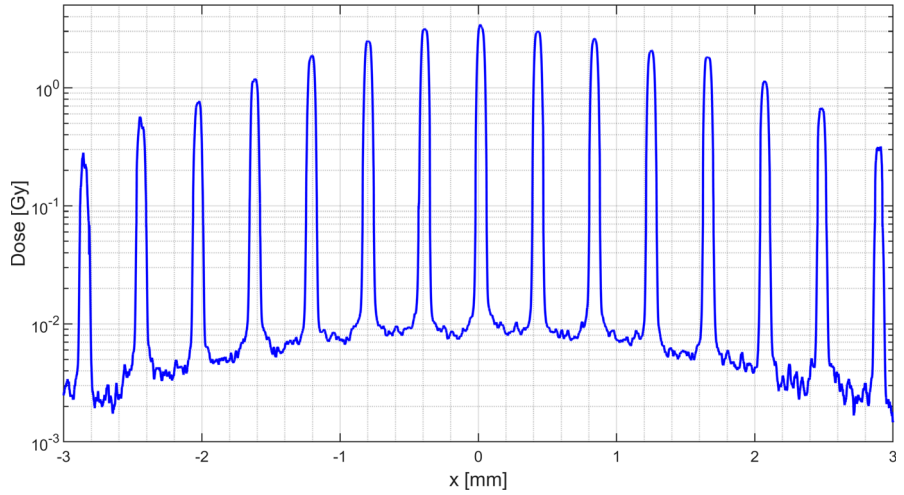

FIG. 6. Full measured dose profile for the grating with 50 μm wide slits. The intensity of the peak doses corresponds to the overall uncollimated beam shape. Due to scattering, intensity of the valley doses shows a broader distribution.

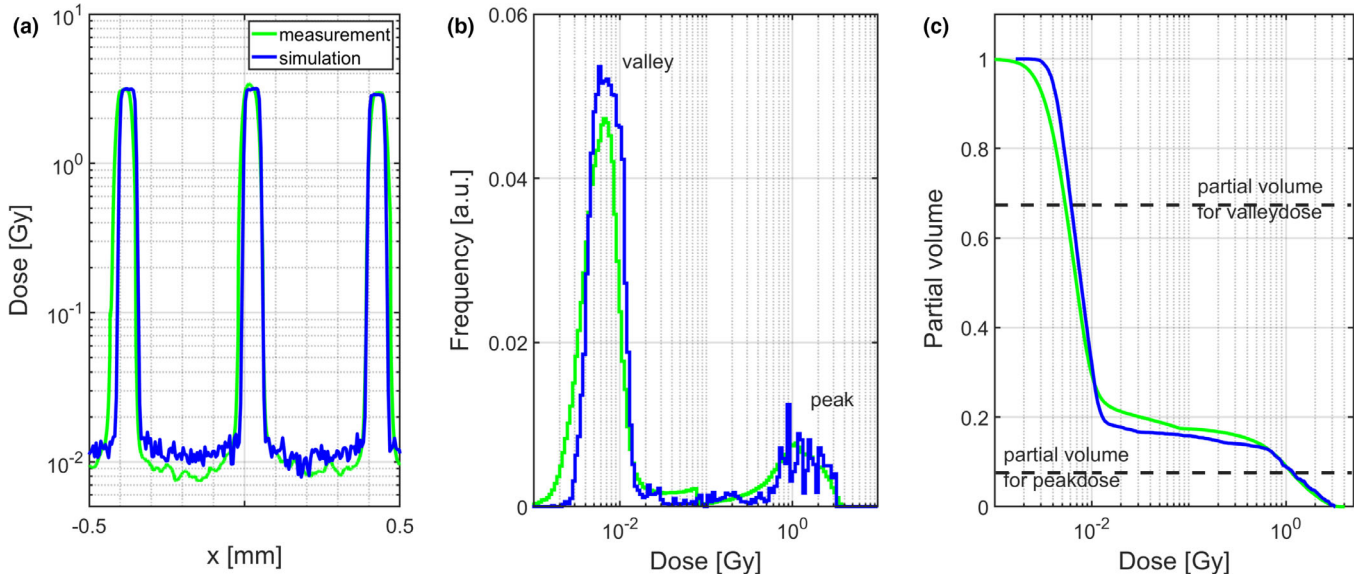

FIG. 7. Measured and simulated dose profiles and histograms. (a) shows the measured (blue) and simulated (green) dose profiles. In (b), the respective dose histograms are plotted, and in (c), the cumulative dose volume histogram used for peak-to-valley dose ratio calculation.

of the total beam area, received at least. The valley dose is defined accordingly as the dose that the peak area plus 60% of the valley area, that is, 1/8+60%·7/8=65% of the total area, received at least [see dotted lines in Fig. 7(c)].

The calculated PVDR from the measured dose distribution is 210 ± 15, from the simulated 190 ± 20. The uncertainty in the simulated dose distributions of about 10% mainly stems from the uncertainties in the underlying physical interaction properties (investigated by using different underlying physics lists). Additionally, the simplified model for the polycapillary optic may also influence the dose distribution.

Hence, the PVDRs in measurement and simulation agree within their uncertainties, indicating a valid simulation and measurement protocol.

3.D. Online dosimetry

Due to machine-intrinsic variations of the photon flux, an online dosimetry system is required to monitor the dose delivery to the sample. It is sufficient to determine the integral dose if the setup components, here the grating absorption and the irradiated material, are well known. A calibrated, relative intensity counter allows to measure the photon counts in front of the irradiation setup. The retrieved photon fluence (photon counts per area) at the photon counting detector was converted to dose D at the sample position by using the mass-energy absorption coefficient of the sample's material,[29] the energy spectrum of the beam, and the geometric positions. This calculation can be used for an open, homogeneous beam. The energy spectrum was computed by Monte Carlo simulation using the parameters of the spectrum measured with an analyzer as given in.[18] The influence of gratings and polycapillary optic on the photon flux was determined before the experiment. We chose to apply a predetermined dose within a quite homogeneously irradiated area, that is, within the FWHM of the focal spot produced by the polycapillary optic (cf. red ellipsoids in Fig. 8). This area is smaller than the one given by the aperture [cf. Fig. 2(e)]. The FWHM of the focal spot was determined by film dosimetry for each irradiation field (circular or quadratic). Taking these parameters into account, the given dose during irradiation can be retrieved from the in-beam intensity counter. The integrated dose value was recalculated by a dedicated script every second to ensure an immediate automated beam interruption as soon as the desired dose was reached.

4. DISCUSSION

We presented the microbeam irradiation system at the MuCLS for *in vivo* treatment of few millimeter-sized, superficial tumors. For the first time, we achieved *in vivo* microbeam irradiations at an inverse Compton scattering source and treated xenograft tumors in the mouse ear.

4.A. Using the MuCLS with polycapillary optic for MRT

Choosing an appropriate beam focusing optic allows to efficiently make use of the available x-ray photons. This is important as high peak doses are required for MRT. Using the optic that yields an ellipsoid focal spot size of $1 \times 1.15 \times \pi\,\mathrm{mm}^2$ instead of the unfocused beam, a 22-fold increase in x-ray intensity was measured. The second available optic providing a minimum focal spot size of $1.65 \times 1.85 \times \pi\,\mathrm{mm}^2$ enhances the intensity by a factor of 11. The presented polycapillary optics are appropriate for the energy range available at the MuCLS. If a future machine design would allow for higher energies, which are desirable for *in vivo* MRT studies due to their higher penetration depth, different focusing options might be required as the efficiency

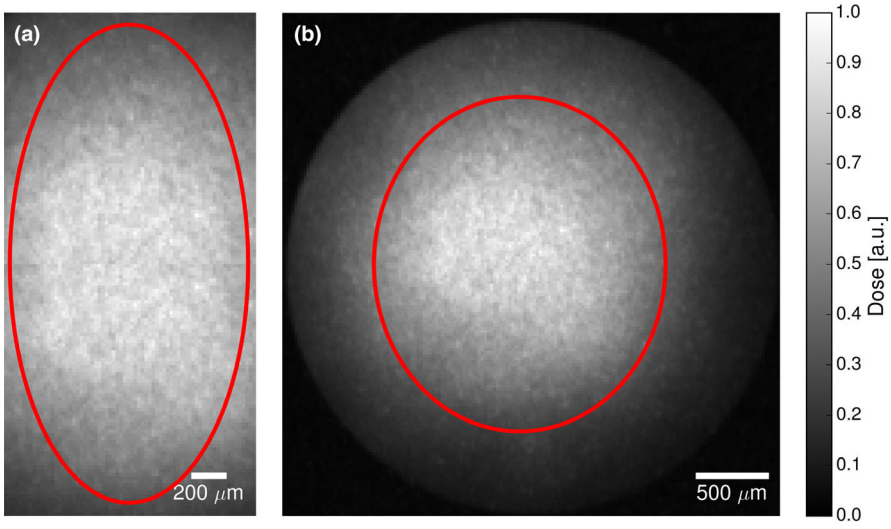

FIG. 8. Measured dose distributions using a polycapillary optic. Scanned radiochromic films show the entire field of view determined by the respectively (a) rectangular or (b) round aperture. The corresponding areas within the full width at half maximum of the Gaussian-shaped dose distribution are indicated by red ellipsoids. Only these areas contribute to the integral dose used for online dosimetry.

of polycapillary optics decreases with energy. Especially, also a monochromatic option could be used. With larger modifications along the beam path, the use of Kirkpatrick–Baez mirrors for 8- to 20-keV x rays could also be considered.[30]

The chosen model of a tumor-bearing mouse ear is well-suited for the small field of view and the low x-ray energy at the MuCLS. Moreover, the tumor is easily kept in place, demonstrated in the corresponding experimental study using γH2AX staining,[23] which is important for the longer irradiation times of up to 1 h at the MuCLS in contrast to the duration of milliseconds to seconds at large-scale synchrotron facilities.[31] If tumors at different positions, for example, in the brain, shall be treated, brain motion due to the heart beat might alter the microbeam pattern.[13] A study with similar dose rates as available at the MuCLS has shown successful brain irradiation of mice using image guidance.[32] Another option to control the irradiation position would be cardiac and respiratory gating. To compare our results with existing studies, one has to take into account the influence of long irradiation times on the early mechanisms for blood vessel repair triggered upon microbeam irradiation. With the current dose rate, microbeam peak doses of several tens of Gy are achievable. A peak dose above 100 Gy would be desirable in order to reach vessel ruptures in the tumor, which is considered to be one of the main reasons for the therapeutic effect of MRT.[1,33] Yet, several studies also showed vascular changes like a reduced blood flow below 100 Gy.[34,35] Upcoming experiments may benefit from higher dose rates due to upgrades of the CLS system. In addition, a future machine design could make available a larger number of photons at the expense of a broader energy bandwidth which is acceptable for MRT treatment.

4.B. Setup for *in vivo* irradiations

The current microbeam irradiation setup at the MuCLS allows to treat few millimeter-sized tumors with tungsten gratings of typical microbeam patterns, for example, 50 μm wide slit spaced by 350 μm tungsten. Depending on shape and size of the tumor, different apertures can be chosen. Furthermore, the irradiation area may be enlarged and adapted to the tumor by patching several irradiation fields with high precision. A polycapillary optic that creates a larger focal spot would optimize the irradiation time, instead of using many sequentially irradiated patched fields. Treating a tumor in the mouse ear, the camera-based positioning system can rely on the transparency of the sample. In case of an opaque sample, such as a tumor in the hind leg, the positioning could be realized using markers and placing the camera in front of the sample in beam direction. Using the imaging system at the MuCLS (absorption and phase-contrast imaging[20,37]), the measurement of tumor position and distribution could even be integrated in the system.

Continuous supervision of the mouse and its body temperature have been installed. For irradiations longer than 1 h, a ventilation equipment is available for the use of gas anesthesia.

4.C. Microbeam characterization

The dose distributions determined in experiment and simulation were found to agree well within the expected uncertainties, indicating a valid simulation and measurement protocol. Yet, no scattering materials were taken into account upstream. For deeper seated tumors, the PVDR will be lower due to scattering in the surrounding tissue. Therefore, the actual PVDR within a tumor cannot be measured but only simulated knowing the depth and composition of the surrounding material. The established protocol paves the way to perform dose planning for future preclinical experiments, especially considering deeper seated tumors. The PVDR for the here-shown experiment at the MuCLS at around 200 is significantly higher than the PVDR of about 20 applied at the ESRF.[38] However, as mentioned above, the PVDR at the MuCLS will also be lower for tumors situated within surrounding tissue.

The high PVDRs achieved here can be used for further studies regarding the influence of the PVDR on overall tumor control and tissue sparing. This might allow to specify useful parameters for MRT treatment, performing a systematic study of PVDR and microbeam size for the tumor model in the mouse ear (extending studies described, for example, in Refs. [39,40]). To compare the results to previous experiments at the ESRF with lower PVDR, the microbeam irradiation at the MuCLS can simply be followed by a homogeneous one. Due to the small field of view at the current microbeam irradiation setup, we used microbeams instead of beams wider than 100 μm, so-called minibeams (e.g., Ref. [41]). With the larger field of view achieved by field patching, a future study could investigate the therapeutic effect of minibeams in small animals.

4.D. Online dosimetry

We successfully commissioned an online dosimetry system at the MuCLS to control the dose delivery during irradiation. A dedicated irradiation software is available to monitor and interrupt dose delivery when necessary. Moreover, it allows to continue irradiation following any interruption (e.g., short interruptions of x-ray delivery, insufficient anesthesia, failure of CLS system). This dosimetry system is well-suited to compare relative doses, for example, when using the same mean dose for microbeam and homogeneous treatment. The system was optimized to deliver the desired dose within a relative standard deviation of 1%.

Yet, taking into account the absorption of different objects along the beam path like windows, gratings, and the sample introduces errors into the absolute dose calculation. Possible reasons are uncertainties of absorption coefficients in available data bases (e.g., Ref. [42,43]). Moreover, we measured a quite large difference of 20% between dose determination via photon counting and film dosimetry. While up to 10% of the error can result from uncertainties of absorption coefficients and the spectrum used for dose calculation, additional smaller errors may be introduced by ionization chamber dosimetry

for film calibration. To reduce these errors in the absolute dose in future experiments, one approach is to replace the relative intensity counter by a transmission chamber calibrated for the conditions at the MuCLS.

5. CONCLUSION

We successfully commissioned a technical setup for *in vivo* microbeam irradiations at a laboratory-sized inverse Compton source, including dosimetry. Thus, this promising tumor therapy modality can now be studied in a preclinical scenario at the MuCLS in order to contribute to the understanding of the radiobiological effect of MRT.

ACKNOWLEDGMENTS

We acknowledge financial support through the DFG Gottfried Wilhelm Leibniz program, the DFG Cluster of Excellence Munich-Centre for Advanced Photonics (MAP) and the Centre for Advanced Laser Applications (CALA). The authors thank for the support by the COST Action TD1205 "SYRA3." Open access funding enabled and organized by Projekt DEAL.

CONFLICTS OF INTEREST

The authors have no conflicts to disclose.

[a]Author to whom correspondence should be addressed. Electronic mail: wilkens@tum.de.

REFERENCES

1. Sabatasso S, Laissue JA, Hlushchuk R, et al. Microbeam radiation-induced tissue damage depends on the stage of vascular maturation. *Int J Radiat Oncol Biol Phys*. 2011;80:1522–1532.
2. Bouchet A, Lemasson B, Le Duc G, et al. Preferential effect of synchrotron microbeam radiation therapy on intracerebral 9L gliosarcoma vascular networks. *Int J Radiat Oncol Biol Phys*. 2010;78:1503–1512.
3. Laissue JA, Bartzsch S, Blattmann H, et al. Response of the rat spinal cord to X-ray microbeams. *Radiother Oncol*. 2013;106:106–111.
4. Bouchet A, Lemasson B, Christen T, et al. Synchrotron microbeam radiation therapy induces hypoxia in intracerebral gliosarcoma but not in the normal brain. *Radiother Oncol*. 2013;108:143–148.
5. Serduc R, Bouchet A, Bräuer-Krisch E, et al. Synchrotron microbeam radiation therapy for rat brain tumor palliation-influence of the microbeam width at constant valley dose. *Phys Med Biol*. 2009;54:6711–6724.
6. Dilmanian FA, Qu Y, Feinendegen LE, et al. Tissue-sparing effect of x-ray microplanar beams particularly in the CNS: Is a bystander effect involved? *Exp Hematol*. 2007;35:69–77.
7. Dilmanian F, Qu Y, Liu S, et al. X-ray microbeams: tumor therapy and central nervous system research. *Nucl Instrum Methods Phys Res Sect A Accel Spectrom Detect Assoc Equip*. 2005;548:30–37.
8. Serduc R, Vérant P, Vial J-C, et al. In In vivo two-photon microscopy study of short-term effects of microbeam irradiation on normal mouse brain microvasculature. *Int J Radiat Oncol*. 2006;64:1519–1527.
9. Brauer-Krisch E, Serduc R, Siegbahn EA, etal. Effects of pulsed, spatially fractionated, microscopic synchrotron X-ray beams on normal and tumoral brain tissue. *Mutat Res*. 2010;704(1-3):160–166.
10. Brönnimann D, Bouchet A, Schneider C, et al. Synchrotron microbeam irradiation induces neutrophil infiltration, thrombocyte attachment and selective vascular damage in vivo. *Sci Rep*. 2016;6:33601.
11. Schültke E, Balosso J, Breslin T, et al. Microbeam radiation therapy - grid therapy and beyond : a clinical perspective. *Br J Radiol*. 2017;90:20170073.
12. Serduc R, Christen T, Laissue J, et al. Brain tumor vessel response to synchrotron microbeam radiation therapy: a short-term in vivo study. *Phys Med Biol*. 2008;53:3609.
13. Duncan M, Donzelli M, Pellicioli P, et al. First experimental measurement of the effect of cardio-synchronous brain motion on the dose distribution during microbeam radiation therapy. *Med Phys*. 2019;47:213–222.
14. Bartzsch S, Cummings C, Eismann S, Oelfke U. A preclinical microbeam facility with a conventional x-ray tube. *Med Phys*. 2016;43:6301–6308.
15. Bruni C, Chiche R, Cizeron R, Fedala Y, Haissinski J. ThomX - Conceptual Design Report, Technical report; 2009. http://hal.in2p3.fr/in2p3-00448278v1. Accessed December 7, 2019.
16. Hadsell M, Cao G, Zhang J, et al. Pilot study for compact microbeam radiation therapy using a carbon nanotube field emission micro-CT scanner. *Med Phys*. 2014;41:061710.
17. Bartzsch S, Oelfke U. Line focus x-ray tubes - a new concept to produce high brilliance x-rays. *Phys Med Biol*. 2017;62:8600.
18. Eggl E, Dierolf M, Achterhold K, et al. The Munich Compact Light Source: initial performance measures. *J Synchrotron Radiat*. 2016;23:1137–1142.
19. Burger K, Ilicic K, Dierolf M, et al. Increased cell survival and cytogenetic integrity by spatial dose redistribution at a compact synchrotron x-ray source. *PLoS One*. 2017;12:e0186005.
20. Achterhold K, Bech M, Schleede S, Potdevin G, Ruth R, Loewen R, Pfeiffer F. Monochromatic computed tomography with a compact laser-driven X-ray source. *Sci Rep*. 2013;3:1313.
21. Oppelt M, Baumann M, Bergmann R, et al. Comparison study of in vivo dose response to laser-driven versus conventional electron beam. *Radiat Environm Biophys*. 2015;54:155–166.
22. Burger K. Microbeam Radiation Therapy at a Compact Synchrotron X-ray Source. PhD thesis, Technical University of Munich, 2017. http://mediatum.ub.tum.de?id=1399928. Accessed March 4, 2019.
23. Dombrowsky AC, Burger K, Porth A-K, et al. A proof of principle experiment for microbeam radiation therapy at the Munich compact light source. *Radiat Environm Biophys*. 2020;59:111–120.
24. Cont D. X-Ray Beam Characterization at the Munich Compact Light Source, Master's thesis. Technical University of Munich; 2016.
25. Richardson WH. Bayesian-based iterative method of image restoration. *J Opt Soc Am*. 1972;62:55–59.
26. Ashland, Gafchromic Radiology, Radiotherapy and Security Radiographic Films, and FilmQA Pro Software; 2017. http://www.gafchromic.com/. Accessed March 4, 2019.
27. Bartzsch S, Lott J, Welsch K, Bräuer-Krisch E, Oelfke U. Micrometer-resolved film dosimetry using a microscope in microbeam radiation therapy. *Med Phys*. 2015;42:4069–4079.
28. Geant4, Physics Reference Manual. https://geant4.web.cern.ch/. Accessed March 4, 2019.
29. Hubbell J, Seltzer S. Tables of X-Ray Mass Attenuation Coefficients and Mass Energy-Absorption Coefficients from 1 keV to 20 MeV for Elements Z = 1 to 92 and 48 Additional Substances of Dosimetric Interest. NISTIR 5632, Technical report, National Institute of Standards and Technology (NIST), Gaithersburg; 1995.
30. Lyncean Technologies Inc. Brochure; 2019. https://lynceantech.com. Accessed June 13, 2019.
31. Bräuer-Krisch E, Nemoz C, Brochard T, et al. The preclinical set-up at the ID17 biomedical beamline to achieve high local dose deposition using interlaced microbeams. *J Phys Conf Ser*. 2013;425:022001.
32. Chtcheprov P, Burk L, Yuan H, et al. Physiologically gated microbeam radiation using a field emission x-ray. *Med Phys*. 2014;41:1–8.
33. Bouchet A, Serduc R, Laissue JA, Djonov V. Effects of microbeam radiation therapy on normal and tumoral blood vessels. *Phys Medica*. 2015;31:634–641.
34. Park HJ, Griffin RJ, Hui S, Levitt SH, Song CW. Radiation-induced vascular damage in tumors: implications of vascular damage in ablative hypofractionated radiotherapy (SBRT and SRS). *Radiat Res*. 2012;177:311–327.
35. Yuan H, Zhang L, Frank JE, et al. Treating brain tumor with microbeam radiation generated by a compact carbon-nanotube-based irradiator: initial radiation efficacy study. *Radiat Res*. 2015;184:322–333.

36. Urban T. Dosimetric Characterization of Microbeams for Preclinical Experiments in Radiotherapy at the Munich Compact Light Source, Master's thesis. Technical University of Munich. 2017.
37. Jud C, Braig E, Dierolf M, et al. Trabecular bone anisotropy imaging with a compact laser-undulator synchrotron x-ray source. *Sci Rep*. 2017;7:14477.
38. Bräuer-Krisch E, Adam J-F, Alagoz E, et al. Medical physics aspects of the synchrotron radiation therapies: Microbeam radiation therapy (MRT) and synchrotron stereotactic radiotherapy (SSRT). *Phys Medica*. 2015;31:568–583.
39. Siegbahn EA. Dosimetry for synchrotron x-ray microbeam radiation therapy, PhD thesis. Technical University of Munich; 2007.
40. Serduc R, Bräuer-Krisch E, Siegbahn EA, et al. High-precision radiosurgical dose delivery by interlaced microbeam arrays of high-flux low-energy synchrotron X-rays. *PLoS ONE*. 2010;5:e902.
41. Prezado Y, Santos MD, Gonzalez W, Jouvion G, Guardiola C, Heinrich S. Transfer of minibeam radiation therapy into a cost-effective equipment for radiobiological studies: a proof of concept. *Sci Rep*. 2017;7:1–10.
42. Tran CQ, Chantler CT, Barnea Z. X-ray mass attenuation coefficient of silicon: theory versus experiment. *Phys Rev Lett*. 2003;90:257401.
43. Andreo P, Burns DT, Salvat F. On the uncertainties of photon mass energy-absorption coefficients and their ratios for radiation dosimetry. *Phys Med Biol*. 2012;57:2117–2136.